

## *Cosmic Himalayas* in *CROCODILE*: Probing the Extreme Quasar Overdensities by Count-in-Cells analysis and Nearest Neighbor Distribution

YUTO KUWAYAMA <sup>1</sup> YONGMING LIANG <sup>2</sup> KENTARO NAGAMINE <sup>1, 3, 4, 5, 6</sup> YURI OKU <sup>7</sup> DAISUKE NISHIHAMA <sup>1</sup>  
DAISUKE TOYOUCHI <sup>1</sup> KEITA FUKUSHIMA <sup>8</sup> HIDENOBU YAJIMA <sup>9</sup> HYUNBAE PARK <sup>9</sup> AND  
MASAMI OUCHI <sup>10, 2, 11, 4</sup>

<sup>1</sup>*Theoretical Astrophysics, Department of Earth and Space Science, The University of Osaka, 1-1 Machikaneyama, Toyonaka, Osaka 560-0043, Japan*

<sup>2</sup>*National Astronomical Observatory of Japan, 2-21-1 Osawa, Mitaka, Tokyo 181-8588, Japan*

<sup>3</sup>*Theoretical Joint Research, Forefront Research Center, Graduate School of Science, The University of Osaka, Toyonaka, Osaka 560-0043, Japan*

<sup>4</sup>*Kavli IPMU (WPI), UTIAS, The University of Tokyo, 5-1-5 Kashiwanoha, Kashiwa, Chiba 277-8583, Japan*

<sup>5</sup>*Department of Physics & Astronomy, University of Nevada, Las Vegas, 4505 S. Maryland Pkwy, Las Vegas, NV 89154-4002, USA*

<sup>6</sup>*Nevada Center for Astrophysics, University of Nevada, Las Vegas, 4505 S. Maryland Pkwy, Las Vegas, NV 89154-4002, USA*

<sup>7</sup>*Center for Cosmology and Computational Astrophysics, the Institute for Advanced Study in Physics, Zhejiang University, China*

<sup>8</sup>*Institute for Data Innovation in Science, Seoul National University, Seoul 08826, Korea*

<sup>9</sup>*Center for Computational Sciences, University of Tsukuba, 1-1-1 Tennodai, Tsukuba, Ibaraki 305-8577, Japan*

<sup>10</sup>*Institute for Cosmic Ray Research, The University of Tokyo, 5-1-5 Kashiwanoha, Kashiwa, Chiba 277-8582, Japan*

<sup>11</sup>*Department of Astronomical Science, SOKENDAI (The Graduate University for Advanced Studies), Mitaka, Tokyo 181-8588, Japan*

### ABSTRACT

The recently reported *Cosmic Himalayas* (CH)—an extreme quasar overdensity at  $z \sim 2$ —poses an apparent challenge to the  $\Lambda$ CDM framework, with a reported significance of  $\delta = 16.9\sigma$  under Gaussian assumptions. Such an event appears improbably rare, with a formal probability of  $P \sim 10^{-68}$ . In this work, we investigate whether CH-like structures can naturally arise in cosmological hydrodynamic simulations. Using the *CROCODILE* simulation, which self-consistently models galaxy–black hole coevolution, we examine quasar clustering through two complementary approaches: the count-in-cells (CIC) statistic, which probes large-scale overdensities, and the nearest-neighbor distribution (NND), sensitive to small-scale environments. CIC analysis reveals that the underlying distribution is heavy-tailed and non-Gaussian, and that conventional Gaussian-based evaluation substantially overestimates the significance of extreme events. When modeled with an asymmetric generalized normal distribution (AGND), the inferred rarity of the CH is substantially reduced and reconciled with standard  $\Lambda$ CDM; for instance, regions appearing as  $12\sigma_{\text{Gauss}}$  outliers under Gaussian assumptions ( $P \sim 10^{-33}$ ) are found to occur in AGND regime with a probability of  $P \sim 10^{-4}$ . NND analysis further demonstrates that extreme overdense regions within the simulation can naturally sustain two-point correlation function values similar to those observed in the CH ( $r_0 \simeq 30 h^{-1}\text{Mpc}$ ), suggesting that the strong clustering stems from sample selection biases and local environmental variations. These two analyses conclusively highlight the importance of adopting non-Gaussian statistics when quantifying extreme overdensities of quasars and establish that the CH is not an anomaly, but a natural outcome of structure formation in the  $\Lambda$ CDM universe.

*Keywords:* Hydrodynamical simulations (767); Cosmology (343); Galaxy evolution (594); High-redshift galaxies (734); Supermassive black holes (1663); Quasars (1319); Cosmological evolution (336); Active galactic nuclei (16); Large-scale structure of the universe (902)

### 1. INTRODUCTION

Understanding the formation of large-scale structures in the early universe is a central goal of modern cosmology (N. Scoville et al. 2007; G. Toni et al. 2025; R. Croft

et al. 2025; M. G. Richarte et al. 2025). Within the Lambda Cold Dark Matter ( $\Lambda$ CDM) paradigm, structure grows hierarchically: small-scale fluctuations collapse first and subsequently merge to form larger systems. One of the most striking manifestations of this process is the emergence of protoclusters at high redshift, the progenitors of today’s galaxy clusters (Y.-K. Chiang et al. 2013; R. A. Overzier 2016). These overdense regions provide unique laboratories for studying the interplay between galaxy assembly, black hole growth, and feedback processes under extreme conditions. Quasar clustering offers a particularly powerful tracer of such environments, as luminous quasars are expected to reside in the most massive halos and thus mark the densest peaks in the cosmic web (C. García-Vergara et al. 2017; M. Mignoli et al. 2020).

A remarkable recent discovery is the “Cosmic Himalayas” (CH), an exceptionally overdense region of quasars identified by Y. Liang et al. (2025). The CH has been interpreted as a protocluster-scale structure (N. A. Hatch et al. 2014; C. García-Vergara et al. 2022; D. Wylezalek et al. 2022), but the reported quasar overdensity of  $\delta = 16.9\sigma$  presents a striking challenge. Under Gaussian assumptions, such an extreme event corresponds to a probability of  $P \sim 10^{-68}$ , far too rare to be expected in a standard  $\Lambda$ CDM universe. This raises a central question: does the CH represent a genuine anomaly that challenges the cosmological model, does it stem from our limited understanding of the complex astrophysical processes governing quasar formation, or does the extraordinary significance arise from limitations in the statistical methods used to quantify overdensity? Resolving this tension is essential for interpreting not only the CH but also the broader role of extreme overdensities in cosmic structure formation.

In this context, cosmological simulations have become indispensable tools. They allow us to investigate structure formation beyond simple analytic approximations, specifically targeting the extreme environments of protoclusters and quasar host regions (e.g., M. Trebitsch et al. 2021). These simulations enable detailed studies of the co-evolution of galaxies, black holes, and the intergalactic medium in overdense regions. At redshifts around  $z \sim 2$ , the epoch of peak cosmic star formation and quasar activity, characterizing high-density regions via simulations provides crucial insight into the earliest stages of cluster assembly (e.g. S. Lim et al. 2021; R.-S. Remus et al. 2023; H. Yajima et al. 2022; M. Andrews et al. 2025). Simulation-based studies reveal a diversity of protocluster evolutionary states and highlight challenges in reproducing the high star-formation rates observed in dense regions (R. A. Overzier 2016). Such

efforts signify the importance of simulations for interpreting extreme overdensities within the  $\Lambda$ CDM framework.

To address this specifically, we analyze the cosmological hydrodynamic simulation *CROCODILE* (Y. Oku & K. Nagamine 2024), which self-consistently models the growth of galaxies and supermassive black holes. This framework allows us to search for CH analogs and to test whether such extreme quasar overdensities can arise naturally within  $\Lambda$ CDM. Identifying these analogs in simulations is also a crucial first step toward exploring their observed correlations with HI gas and Ly $\alpha$  emitters, providing a pathway to investigate quasar feedback on the surrounding intergalactic medium.

Our analysis employs two complementary statistical tools. The count-in-cells (CIC) method provides a one-point statistic that evaluates the distribution of quasar counts across fixed volumes. By constructing the probability distribution  $P_{\text{CIC}}(N; V)$  of counts within cells of size  $V$ , the CIC directly measures deviations from a random (Poisson) distribution and thus probes the statistical rarity of overdense regions (e.g. H. Ueda & J. Yokoyama 1996; A. Yang & W. C. Saslaw 2011; J. Shin et al. 2017). Since CIC was the method used by Y. Liang et al. (2025) to evaluate the CH, it provides a direct point of comparison. Complementing the CIC, the nearest-neighbor distribution (NND) quantifies the distances to the closest quasar pairs and is particularly sensitive to compact structures and dense environments. NND statistics provide a powerful diagnostic of small-scale clustering and local environment (B. S. Ryden & E. L. Turner 1984), and their use has expanded in both cosmology and related fields (A. Banerjee & T. Abel 2021; A. Ouellette & G. Holder 2025; Z. Zhou et al. 2025).

Throughout this work, we assume the cosmological parameters from Planck Collaboration et al. (2020):  $(\Omega_m, \Omega_b, \Omega_\Lambda, h, n_s, 10^9 A_s) = (0.3099, 0.0488911, 0.6901, 0.67742, 0.96822, 2.1064)$ .

The structure of this paper is as follows: Section 2 outlines the simulation setup, Section 3 details the methodology for the CIC and NND analyses and presents the results, Section 4 discusses the emergence of extreme overdense regions of quasars in the context of large-scale observations, and Section 5 summarizes our conclusions.

**Table 1.** Parameter-set of the simulation box of each simulation.

Parameters	Unit	L200N1024 BOOSTFACTOR50 NO EDDINGTON LIMIT (BF50NEL)
Boxsize	$(h^{-1}\text{cMpc})^3$	200 <sup>3</sup>
Target Redshift of this work	-	2.2
Softening length	$h^{-1}\text{ckpc}$	6.76
Maximum softening length	$h^{-1}\text{pkpc}$	1.00
DM mass	$h^{-1}M_{\odot}$	$5.39 \times 10^8$
Gas mass	$h^{-1}M_{\odot}$	$1.01 \times 10^8$
Seed BH mass	$h^{-1}M_{\odot}$	$1 \times 10^5$
$C_{\text{visc}}$	-	200 $\pi$
Boost Factor	-	50
Calculation of BH accretion	-	Angular-momentum-limited Bondi accretion w/o the Eddington accretion limit

## 2. COSMOLOGICAL HYDRODYNAMIC SIMULATION *CROCODILE*

Our analysis is based on the *CROCODILE*<sup>12</sup> v2 suite of cosmological hydrodynamic simulations, performed with the GADGET4-OSAKA smoothed particle hydrodynamics (SPH) code (L. E. C. Romano et al. 2022a,b; Y. Oku & K. Nagamine 2024), which is built upon the publicly available GADGET-4 code (V. Springel et al. 2021)<sup>13</sup>. Detailed descriptions of the gravity and hydrodynamics solvers can be found in V. Springel et al. (2021) and Y. Oku & K. Nagamine (2024).

The initial condition is generated using MUSIC2-MONOFONIC<sup>14</sup> (O. Hahn et al. 2021; M. Michaux et al. 2021). To suppress the impact of cosmic variance, we employed the phase-fixing technique (R. E. Angulo & A. Pontzen 2016). The particles were initialized at  $z_{\text{ini}} = 39$  using third-order Lagrangian perturbation theory (3LPT). The transfer function at  $z_{\text{ini}}$  was obtained by back-scaling the transfer function from a reference redshift of  $z_{\text{ref}} \sim 2$ , computed by CLASS<sup>15</sup> (D. Blas et al. 2011).

The simulation volume is a periodic cubic box of side length  $L_{\text{box}} = 200 h^{-1} \text{cMpc}$ . We employ  $1024^3$  dark matter particles and an initially equal number of gas particles. This configuration corresponds to a dark matter particle mass of  $m_{\text{DM}} = 5.39 \times 10^8 h^{-1} M_{\odot}$  and initial gas particle mass of  $m_{\text{gas}} = 1.01 \times 10^8 h^{-1} M_{\odot}$ . The gravitational softening length is set to  $\epsilon_{\text{grav}} =$

$6.76 h^{-1} \text{ckpc}$ , but limited to physical  $1.00 h^{-1} \text{pkpc}$  at all times.

The simulations incorporate sub-grid prescriptions for key baryonic processes, including star formation, supernova (SN) feedback (Y. Oku et al. 2022), and active galactic nucleus (AGN) feedback (Y. Oku & K. Nagamine 2024). Chemical enrichment is modeled with the CELib library (T. R. Saitoh 2017), which self-consistently tracks the enrichment of multiple elements.

Radiative cooling and heating are computed using the GRACKLE<sup>16</sup> chemistry and cooling library (B. D. Smith et al. 2017). GRACKLE solves a non-equilibrium primordial chemical network including hydrogen, deuterium, helium species, and molecular hydrogen ( $\text{H}_2$ ) and HD. Metal-line cooling is incorporated via precomputed tables from the photoionization code CLOUDY (G. J. Ferland et al. 2013), which account for photoionization and photoheating by the cosmic ultraviolet background (UVB), with self-shielding corrections applied at high density. We adopt the spatially uniform, redshift-dependent UVB model of F. Haardt & P. Madau (2012), which is activated at  $z = 8$ .

### 2.1. BH accretion and AGN feedback model

First, we describe the seeding prescription for black holes (BHs). We employ a method based on the on-the-fly halo identification using the Friends-of-Friends (FoF) algorithm. A seed BH with an initial mass of  $M_{\text{BH}} = 10^5 h^{-1} M_{\odot}$  is placed at the position of the minimum gravitational potential within a halo. Seeds are introduced only in haloes that exceed a threshold mass of  $M_{\text{FoF,seed}} = 10^{10} h^{-1} M_{\odot}$ .

<sup>12</sup> CROCODILE Project: <https://sites.google.com/view/crocodilesimulation/home>

<sup>13</sup> GADGET-4: <https://www.mpa.mpa-garching.mpg.de/gadget4/>

<sup>14</sup> MUSIC2-MONOFONIC: <https://bitbucket.org/ohahn/monofonic/src/master/>

<sup>15</sup> CLASS: <http://class-code.net/>

<sup>16</sup> We use version GRACKLE-3.2.1, see <https://grackle.readthedocs.io/en/grackle-3.2.1/>.

Once seeded, the BH accretion rate,  $\dot{M}_{\text{acc}}$ , is calculated using an angular-momentum-limited Bondi prescription with a resolution-dependent boost factor:

$$\dot{M}_{\text{acc}} = \alpha C \dot{M}_{\text{Bondi}}, \quad (1)$$

where  $\dot{M}_{\text{Bondi}}$  is the Bondi accretion rate, and  $\alpha = 50$  is the boost factor introduced to compensate for the limited spatial resolution and unresolved small-scale physics such as chaotic cold accretion (M. Gaspari et al. 2013). The value  $\alpha = 50$  is chosen to be consistent with previous implementations in the GADGET4-OSAKA simulations, calibrated to reproduce observed BH mass functions and scaling relations. The dimensionless coefficient  $C$  accounts for angular-momentum support and viscous effects in the accretion flow, and is defined as (Y. M. Rosas-Guevara et al. 2015; Y. Oku & K. Nagamine 2024)

$$C = \min \left[ C_{\text{visc}}^{-1} \left( \frac{c_s}{v_\phi} \right)^3, 1 \right], \quad (2)$$

where  $c_s$  is the sound speed of the ambient gas,  $v_\phi$  is the rotational velocity of the gas around the BH, and  $C_{\text{visc}} = 200\pi$  is a calibration parameter. The underlying Bondi accretion rate is given by

$$\dot{M}_{\text{Bondi}} = \frac{4\pi G^2 M_{\text{BH}}^2 \rho}{c_s^3} \quad (3)$$

where  $\rho$  is the local gas density.

In the fiducial *CROCODILE* runs, BH growth is capped at the Eddington limit. In this work, however, we adopt a model without this restriction (“NEL”; No-Eddington-Limit), allowing for brief episodes of super-Eddington accretion, a scenario supported by recent observational detections of super-Eddington AGNs (e.g., H. Suh et al. 2025). This choice is motivated by the shortcomings of the Eddington-limited model, which tends to overproduce AGN by failing to sufficiently quench low-mass BHs. By enabling short bursts of rapid growth, the NEL model generates more energetic feedback events that effectively suppress accretion in less massive BHs, while simultaneously allowing the most massive BHs to reach the high accretion rates required to reproduce the observed Eddington ratio distribution and luminous quasar population at high redshift. As shown in Sec. 3.4, this approach yields a BH population in much better agreement with observational constraints.

Feedback from BH accretion is implemented as purely thermal AGN feedback, following the EAGLE scheme as adopted in *CROCODILE* (J. Schaye et al. 2015; R. A. Crain et al. 2015; Y. Oku & K. Nagamine 2024). A fixed

fraction of the accreted rest-mass energy is coupled to the surrounding gas:

$$\dot{E}_{\text{AGN}} = \epsilon_f \epsilon_r \dot{M}_{\text{acc}} c^2, \quad (4)$$

where  $\epsilon_r = 0.1$  is the radiative efficiency and  $\epsilon_f = 0.15$  is the feedback efficiency (see Table 1 of Y. Oku & K. Nagamine 2024). The energy is injected stochastically into neighboring gas particles as thermal energy, a method designed to avoid numerical overcooling. This prescription has been shown to reproduce observed galaxy–BH scaling relations and provides a physically motivated mechanism for regulating BH growth and quasar feedback in cosmological simulations.

We also updated the treatment of the sound speed  $c_s$  in the accretion model between version 1 (“V1”; Y. Oku & K. Nagamine 2024) and version 2 (“V2”; Nishihama et al., in prep.) In V1, we calculated  $c_s$  using only the temperature derived from the effective equation of state (EoS) employed in the EAGLE simulation (J. Schaye et al. 2015; R. A. Crain et al. 2015):

$$c_{s,\text{EoS}} = \sqrt{\gamma \frac{k_B}{\mu_a m_p} T_{\text{EoS}}} \quad (5)$$

where  $\gamma = 5/3$  is the adiabatic index,  $k_B$  is the Boltzmann constant,  $\mu = 1.2285$  is the mean molecular weight of primordial atomic gas, and  $m_p$  is the proton mass. The effective temperature is given by  $T_{\text{EoS}} = 8 \times 10^3 \text{ K} (n_{\text{H}}/0.1 \text{ cm}^{-3})^{1/3}$ . This formulation in V1 was based on the simplified assumption that BHs always accrete from the star-forming ISM governed by this polytropic EoS.

In V2, we modified this implementation to align with the standard strategy of the EAGLE simulation, where the effective EoS serves as a lower limit (i.e., a temperature floor) for the gas temperature. Specifically, V2 adopts the larger of the EoS temperature and the actual thermodynamic gas temperature  $T_{\text{gas}}$ :

$$c_s = \sqrt{\gamma \frac{k_B}{\mu_a m_p} T_{\text{v2}}}, \quad (6)$$

$$T_{\text{v2}} = \max(T_{\text{EoS}}, T_{\text{gas}}), \quad (7)$$

where  $T_{\text{gas}}$  denotes the thermodynamic temperature of the local gas surrounding the BH. This prescription effectively prevents unphysically high Bondi accretion rates in cold, dense gas while accounting for the thermal state of gas hotter than the effective EoS. Consequently, the Bondi rate is more strongly suppressed in such regions, resulting in systematically weaker AGN feedback than in V1. A complete list of the adopted simulation parameters is provided in Table 1.

In practice, this refinement defines the V2 accretion model. For the present study, we employ the BF50NEL run, which combines the V2 prescription with the allowance for super-Eddington accretion. Together, these features are crucial for reproducing the observed abundance of luminous quasars at high redshift (Figures 1–3), making our simulation a robust framework for investigating extreme structures such as the Cosmic Himalayas.

### 3. ANALYSIS METHODS AND RESULTS

Before detailing the black hole and luminosity selections, we first outline the overall strategy for ensuring a consistent comparison between the simulation and the observations.

#### 3.1. Normalization of quasar number density and methodological overview

The observed mean quasar number per  $L_{\text{cell}} \simeq 30 h^{-1} \text{Mpc cell}$ ,  $\bar{N}_{\text{SDSS}} = 0.36$ , is derived from the SDSS, which covers a comoving Gpc-scale volume and therefore provides a robust estimate of the cosmic mean density of luminous quasars at  $z \sim 2$  (Y. Liang et al. 2025). To enable a meaningful comparison, we apply two quasar selection criteria for our simulation samples. These selection criteria significantly alter cosmic quasar number densities, and varying selections allow us to quantify the sensitivity of the results to the sample selection and assess the impact of different levels of bias.

The fiducial selection criterion (Case A) gives us a similar number density as the SDSS samples ( $\bar{N}_{\text{QSO}} \sim 0.25$  in  $L_{\text{cell}} = 30 h^{-1} \text{Mpc cells}$ ), as we describe in Section 3.3. On the other hand, the Case B criterion covers a slightly wider BH mass range than the SDSS samples, resulting in a higher number density than in the SDSS sample ( $\bar{N}_{\text{QSO}} \sim 1.5$  in  $L_{\text{cell}} = 30 h^{-1} \text{Mpc cells}$ ).

First, we perform the CIC analysis. This characterizes the global distribution and statistical rarity of extreme overdensities such as the CH. For the CIC analysis, a quasar selection criterion sets the mean of the probability distribution  $P_{\text{CIC}}(N_{\text{QSO}}; L_{\text{cell}})$  when fitting analytic models such as the asymmetric generalized normal distribution (AGND), while still allowing the higher moments (variance, skewness, and tail shape) to reflect the intrinsic clustering in the simulation.

Second, we perform the NND analysis, which directly compares the small-scale clustering of extreme overdensities. This allows us to measure the clustering properties as a probability distribution for finding the nearest neighbors  $P_{\text{NN}}(< r)$ .

Although the finite volume of the *CROCODILE* box ( $L_{\text{box}} = 200 h^{-1} \text{Mpc}$ ) introduces cosmic variance in the

estimate of  $\bar{N}_{\text{QSO}}$ , this does not bias the NND analysis, as the normalization ensures consistency with the observationally determined mean density. The two statistical measures, therefore, play complementary roles: the CIC quantifies the global distribution and non-Gaussianity, whereas the NND measures the small-scale clustering of quasar overdensities.

To further validate the robustness of our results against box-size limitations, we performed an independent CIC analysis using the *Uchuu* simulation (T. Ishiyama et al. 2021), which spans a much larger comoving volume of  $L_{\text{box}} = 2 h^{-1} \text{Gpc}$ . As presented in Appendix A, this analysis confirms that the non-Gaussian shape of the CIC distribution persists on Gpc scales. This cross-check demonstrates that the conclusions drawn from our fiducial simulation are not artifacts of limited volume, but reflect generic statistical properties of the quasar population within the  $\Lambda\text{CDM}$  framework.

#### 3.2. Luminosity Estimation of Black hole

We estimate the bolometric luminosities of AGNs ( $L_{\text{bol}}$ ) as follows:

$$L_{\text{bol}} = \epsilon_r \dot{M}_{\text{BH}} c^2, \quad (8)$$

where  $\epsilon_r = 0.1$  is the radiative efficiency in the *CROCODILE* feedback model.

To construct the X-ray luminosity function (XLF) of AGN, we also estimate the hard X-ray (2–10 keV) luminosity  $L_{\text{X}}$  from  $L_{\text{bol}}$ . For this conversion, we employ the bolometric correction model of P. F. Hopkins et al. (2007), defined as

$$\log_{10} \left( \frac{L_{\text{X}}}{L_{\odot}} \right) = \log_{10} \left( \frac{L_{\text{bol}}}{L_{\odot}} \right) - \log_{10} \text{BC}, \quad (9)$$

$$\text{BC} = 10.83 \left( \frac{L_{\text{bol}}}{10^{10} L_{\odot}} \right)^{0.28} + 6.08 \left( \frac{L_{\text{bol}}}{10^{10} L_{\odot}} \right)^{-0.020}, \quad (10)$$

where  $L_{\odot}$  is the solar luminosity, and BC is the bolometric correction factor from  $L_{\text{bol}}$  to  $L_{\text{X}}$ .

#### 3.3. Selection Criteria for Quasars from the Simulation

In our analysis, luminous AGNs are identified as BHs that satisfy both mass and luminosity thresholds. We adopt two alternative sets of selection criteria, denoted as Case A and Case B. The conditions are summarized below:

**Table 2.** Parameter sets and the results of CIC and NND analyses

Simulation		Selection Criteria	$L_{\text{cell}} [h^{-1} \text{ cMpc}]$	$\bar{N}_{\text{CIC}}$	$N_{\text{CIC}}^{\text{max}}$	$r_0 [h^{-1} \text{ cMpc}]$
Case A	<i>CROCODILE</i>	$8.0 \leq \log_{10}(M_{\text{BH}}/M_{\odot}) \leq 9.5,$ $\log_{10}(L_{\text{bol}}/\text{erg s}^{-1}) > 45.47$ w/ Type II reduction (A. Merloni et al. 2014)	30	0.25	6	30.9
Case B	<i>CROCODILE</i>	$7.1 \leq \log_{10}(M_{\text{BH}}/M_{\odot}) \leq 9.9,$ $\log_{10}(L_{\text{bol}}/\text{erg s}^{-1}) > 45$ w/ Type II reduction (A. Merloni et al. 2014)	30	1.5	17	13.7
Case C	<i>Uchuu</i> (Appendix A)	$\log_{10}(M_{200c}/M_{\odot}) > 11.5$ w/ AGN selection (S. B. Rembold et al. 2023)	30	0.36	9	–

$$8.0 \leq \log_{10} \left( \frac{M_{\text{BH}}}{M_{\odot}} \right) \leq 9.5 \quad (\text{case A}) \quad (11)$$

$$\log_{10} \left( \frac{L_{\text{bol}}}{\text{erg s}^{-1}} \right) > 45.47 \quad (\text{case A}) \quad (12)$$

$$7.1 \leq \log_{10} \left( \frac{M_{\text{BH}}}{M_{\odot}} \right) \leq 9.9 \quad (\text{case B}) \quad (13)$$

$$\log_{10} \left( \frac{L_{\text{bol}}}{\text{erg s}^{-1}} \right) > 45 \quad (\text{case B}). \quad (14)$$

Case A represents a narrower selection, with a BH mass range consistent with the  $1\sigma$  scatter of SDSS quasars at  $z \sim 2$  (S. Rakshit et al. 2020) and a luminosity threshold comparable to that of the quasars identified in the CH (Y. Liang et al. 2025).

Case B, by contrast, adopts a broader mass interval consistent with the  $3\sigma$  scatter of SDSS quasars together with a luminosity threshold reflecting the  $2\sigma$  range of the SDSS quasar population at  $z \sim 2$ . These dual selections allow us to determine the extent to which varying the sample bias influences the resulting clustering properties. Together, these two complementary definitions bracket the observational uncertainties, enabling a systematic evaluation of whether CH analogs can naturally arise within the  $\Lambda$ CDM framework.

For the luminous AGNs, we select Type I AGNs from the total sample via random selection based on the Type I fraction model from A. Merloni et al. (2014):

$$f_{\text{Type I}} = A - \frac{1}{\pi} \arctan \left( \frac{l_0 - l_x}{\sigma_x} \right) \quad (15)$$

where  $l_x = \log_{10} L_X$ ,  $A = 0.44$ ,  $l_0 = 43.89$ ,  $\sigma_x = 0.46$ . This model introduces stochasticity. To account for this sample-selection uncertainty, we generated 100 independent realizations of the Type I AGN sample via random sampling and analyzed the results based on the ensemble in each case. Table 2 summarizes the selection criteria and the corresponding analysis results for each case.

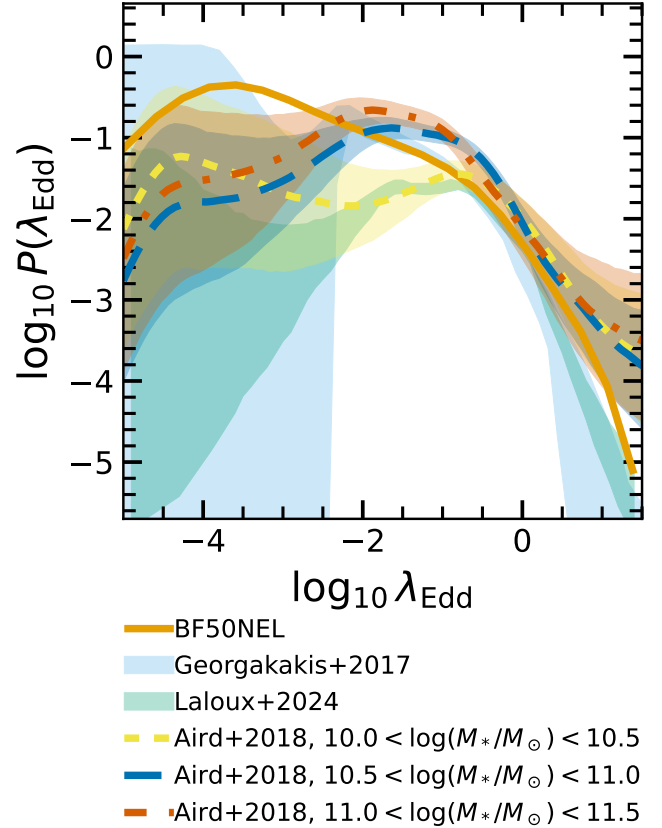


**Figure 1.** Eddington ratio ( $\lambda_{\text{Edd}}$ ) distribution function for BHs in our simulation BF50NEL (solid orange line). Colored lines and shaded regions indicate observational constraints: sky blue and green shades correspond to A. Georgakakis et al. (2017) ( $z = 2.25$ ) and B. Laloux et al. (2024) ( $1.5 < z < 2.0$ ), respectively, while yellow, blue, and thick orange dotted lines with shades represent the constraints in stellar mass bins of J. Aird et al. (2018) ( $2.0 < z < 2.5$ ).

### 3.4. AGN properties in *CROCODILE*

To clarify the BH properties in our simulation, we examine the Eddington ratio distribution function (ERDF) (Eddington ratio;  $\lambda_{\text{Edd}} \equiv \dot{M}_{\text{BH}}/\dot{M}_{\text{Edd}}$ ), the X-ray luminosity function (XLF), and the BH mass func-

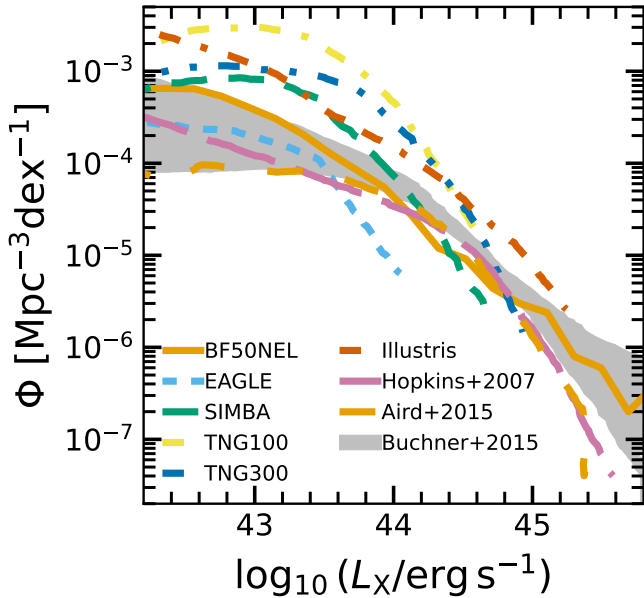


**Figure 2.** X-ray luminosity function (XLF) from simulations and observations. The orange solid line shows the result from our BF50NEL simulation. Colored dotted curves indicate results from other simulation projects compiled by M. Habouzit et al. (2022): EAGLE (sky blue; J. Schaye et al. 2015; R. A. Crain et al. 2015), SIMBA (green; R. Davé et al. 2019), TNG100 (yellow) and TNG300 (blue; D. Nelson et al. 2018), and Illustris (red; M. Vogelsberger et al. 2014). Observational estimates are shown from P. F. Hopkins et al. (2007) (pink), J. Aird et al. (2015) (orange dotted line), and J. Buchner et al. (2015) (gray shade).

tion (BHMF), and compare them with both observational data and other simulation results.

Figure 1 presents the ERDF measured from our BF50NEL run, alongside several observational estimates. The observational constraints are taken from A. Georgakakis et al. (2017), B. Laloux et al. (2024), and J. Aird et al. (2018), corresponding to redshift ranges  $z = 2.25$  (A. Georgakakis et al. 2017),  $1.5 < z < 2.0$  (B. Laloux et al. 2024), and  $2.0 < z < 2.5$  (J. Aird et al. 2018), respectively. For J. Aird et al. (2018), we show results in three stellar mass bins:  $10.0 < \log_{10}(M_*/M_\odot) < 10.5$ ,  $10.5 < \log_{10}(M_*/M_\odot) < 11.0$ , and  $11.0 < \log_{10}(M_*/M_\odot) < 11.5$ .

Notably, the ERDF of our BF50NEL run (Figure 1) shows excellent agreement with these observational constraints, particularly in the high-Eddington-ratio regime (i.e.,  $\log_{10} \lambda_{\text{Edd}} \gtrsim -2.5$ ). This consistency indicates that our model successfully reproduces the population of bright, actively accreting BHs that are relevant to the quasar activity discussed in this work.

Figure 2 presents the X-ray luminosity function (XLF) from our simulation, compared with both observational data and results from other large cosmological simula-

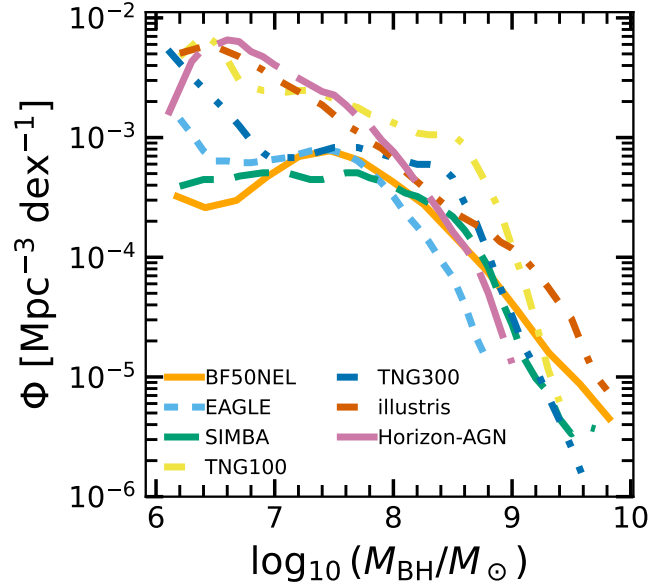
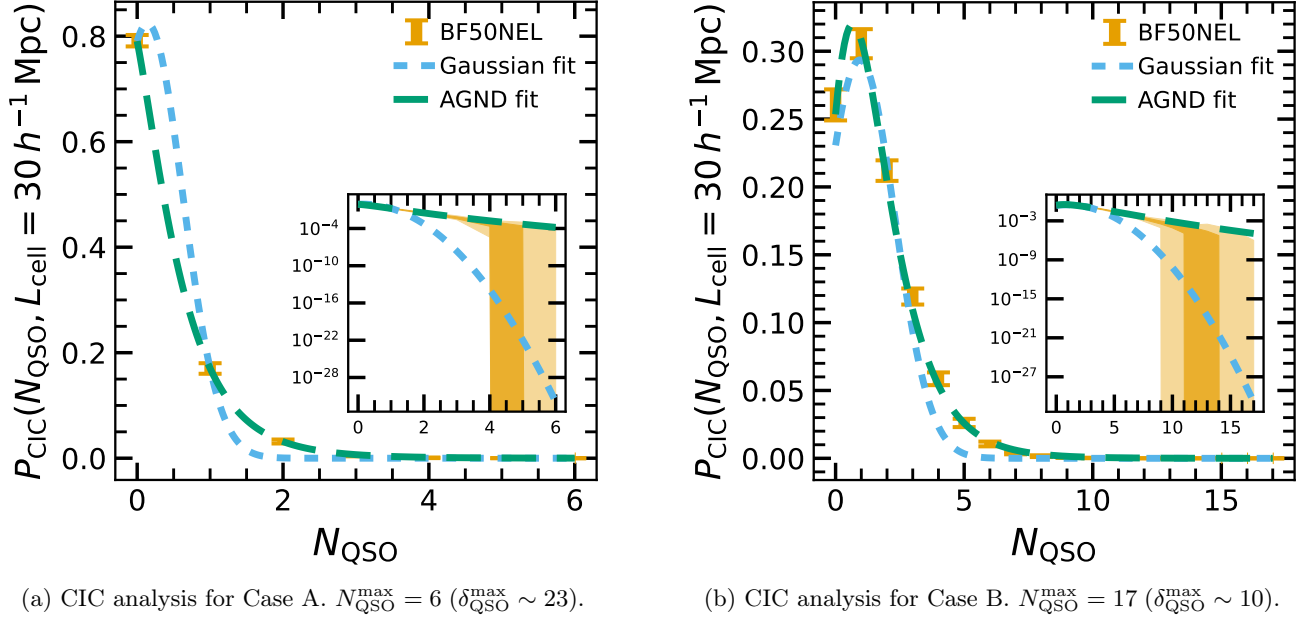


**Figure 3.** Black hole mass function (BHMF) from simulations. The orange solid line shows the result from our BF50NEL simulation. Other colored curves represent results from major cosmological hydrodynamic simulations compiled by M. Habouzit et al. (2021): EAGLE (sky blue; J. Schaye et al. 2015; R. A. Crain et al. 2015), SIMBA (green; R. Davé et al. 2019), TNG100 (yellow) and TNG300 (blue; D. Nelson et al. 2018), Illustris (red; M. Vogelsberger et al. 2014), and Horizon-AGN (pink; Y. Dubois et al. 2014).

tions. The comparison simulation results are taken from the analysis of M. Habouzit et al. (2022): EAGLE (J. Schaye et al. 2015; R. A. Crain et al. 2015), SIMBA (R. Davé et al. 2019), TNG100 and TNG300 (D. Nelson et al. 2018), and Illustris (M. Vogelsberger et al. 2014). Crucially, we estimate the hard X-ray luminosity (2–10 keV) applying the bolometric correction of P. F. Hopkins et al. (2007), consistent with the methodology of M. Habouzit et al. (2022). The observational constraints shown are from P. F. Hopkins et al. (2007), J. Aird et al. (2015), and J. Buchner et al. (2015).

The XLF of our BF50NEL run (Figure 2) shows good agreement with the J. Buchner et al. (2015) results at  $\log_{10}(L_X/\text{erg s}^{-1}) \lesssim 44$  and  $\log_{10}(L_X/\text{erg s}^{-1}) \gtrsim 44.8$ , though it slightly underestimates the number densities in the intermediate range  $44 \lesssim \log_{10}(L_X/\text{erg s}^{-1}) \lesssim 44.8$ .

Figure 3 shows the BH mass function (BHMF) from our simulation, together with other simulations analyzed by M. Habouzit et al. (2021): the same set as in the XLF comparison (EAGLE, SIMBA, TNG100, TNG300, and Illustris), along with Horizon-AGN (Y. Dubois et al. 2014).



(a) CIC analysis for Case A.  $N_{\text{QSO}}^{\text{max}} = 6$  ( $\delta_{\text{QSO}}^{\text{max}} \sim 23$ ).

(b) CIC analysis for Case B.  $N_{\text{QSO}}^{\text{max}} = 17$  ( $\delta_{\text{QSO}}^{\text{max}} \sim 10$ ).

**Figure 4.** Count-in-cells (CIC) probability distribution of quasars for  $L_{\text{cell}} = 30 h^{-1} \text{Mpc}$ . The orange error bars show the CIC measured from our simulation (BF50NEL), which corresponds to the scatter obtained from the 100 jackknife trials of Type I AGN realization. The blue dashed curve corresponds to a Gaussian fit, while the green long-dashed curve shows the AGND fit. The inset panel presents the same distributions on a semi-log scale, highlighting the deviations between the Gaussian model and the simulation results in the high- $N_{\text{QSO}}$  regime. The deep orange shade of the inset panel shows the  $1\sigma$  scatter of the CIC across the 100 jackknife trials (16th–84th percentiles). In contrast, the pale orange shade shows the full range of the scatter. Since the extreme overdense regions (e.g.,  $N_{\text{QSO}} \geq 5$  for Case A) do not appear in every selection, the minimum probability often reaches zero. When plotted on a semi-log scale, this results in the shade having an artificially large vertical extent, as the lower bound effectively extends down to the axis limit.

The BHMF from our simulation (Figure 3) agrees well with other simulations for  $\log_{10}(M_{\text{BH}}/M_{\odot}) \gtrsim 7.0$ , further confirming the robustness of our BH modeling.

Overall, these comparisons demonstrate that the BH population in our simulation is consistent with both observations and other state-of-the-art simulations. This provides a solid and reliable foundation for the subsequent quasar clustering analyses presented in this work.

### 3.5. Count-in-cells (CIC) analysis

We perform a count-in-cells (CIC) analysis, a statistical method widely used to quantify the spatial distribution of objects such as galaxies (e.g., H. Ueda & J. Yokoyama 1996; A. Yang & W. C. Saslaw 2011; J. Shin et al. 2017). The CIC is a one-point statistic that characterizes the probability distribution of object counts within fixed spatial volumes  $V$  (“cells”). In practice, the survey or simulation volume is partitioned into cells of a chosen size, typically centered on grid nodes and allowing overlap, and the number of objects  $N$  within each cell is recorded. From the ensemble of counts, the probability distribution function  $P_{\text{CIC}}(N; V)$  is then constructed.

The shape of  $P_{\text{CIC}}(N; V)$  provides a sensitive probe of cosmic structure. Deviations from a purely random

(Poisson) distribution signal the presence of clustering, while the tails of the distribution capture rare overdense or underdense regions. As such, CIC analysis is a powerful tool for quantifying the clustering of objects and for detecting non-Gaussian signatures in the underlying density field, which encode key information about structure formation and the nature of gravity.

We employ the CIC analysis to characterize both the shape of  $P_{\text{CIC}}(N; V)$  and the probability of extreme overdense regions within our simulation. In this work, we define each cell as a sub-box of size  $L_{\text{cell}} = 30 h^{-1} \text{Mpc} = 44.3 \text{Mpc}$  (for  $h = 0.67742$ ; comoving), which is close to what Y. Liang et al. (2025) took. From the full simulation volume ( $L = 200 h^{-1} \text{cMpc}$ ), we randomly select  $10^6$  such cells. This random sampling approach enables us to identify quasar overdensities that a purely grid-based cell placement might miss.

Figure 4 presents the resulting CIC distributions, together with fitted models. We consider both a Gaussian function and the asymmetric generalized normal distribution (AGND) as fitting forms.

The Gaussian model is characterized by two parameters: mean and standard deviation. In contrast, the AGND model naturally accommodates skewness and asymmetry in the distribution, providing a better rep-

**Table 3.** Best-fit parameters of the Gaussian model and the asymmetric generalized normal distribution (AGND) model for the quasar CIC PDF.

Gaussian	$\mu$	$\sigma$	AGND	$\alpha$	$\kappa$	$\xi$
Case A	0.140	0.484	Case A	0.525	0.5444	0.0405
Case B	0.944	1.358	Case B	1.37	0.441	1.217

resentation of the CIC results, as demonstrated in Figure 4. The AGND model is specifically designed to capture non-Gaussian features in probability distributions and has previously been employed for CIC analyses by J. Shin et al. (2017). We adopt the notation  $\mathcal{N}_{v2}$  following their designation of this function as the ‘generalized normal distribution version 2’. Its functional form is

$$\mathcal{N}_{v2}(x) = \frac{\mathcal{N}(y)}{\alpha + \kappa(x - \xi)}, \quad (16)$$

$$y = \begin{cases} \frac{1}{\kappa} \ln \left[ 1 + \frac{\kappa(x - \xi)}{\alpha} \right] & (\kappa \neq 0), \\ \frac{x - \xi}{\alpha} & (\kappa = 0), \end{cases} \quad (17)$$

where  $\mathcal{N}(y)$  denotes the Gaussian distribution. The three free parameters have intuitive interpretations:  $\alpha$  sets the overall width of the distribution,  $\xi$  specifies its location (analogous to the median), and  $\kappa$  controls the degree of asymmetry. This flexibility allows the AGND to reproduce the skewed, heavy-tailed shapes that characterize the CIC distributions in our simulation and to provide a physically meaningful alternative to Gaussian fits.

As shown in Figure 4, the Gaussian fit fails to reproduce both the skewness and the high-density tail of the CIC distribution in both Cases. Furthermore, based on the Gaussian fit results, regions corresponding to  $12\sigma_{\text{Gauss}}$  overdensities (representing the highest overdensities observed in both Case A and Case B) are found to appear naturally in the simulation. While both samples reach this same statistical significance level relative to the Gaussian fit, the corresponding physical overdensities differ markedly: Case A reveals extremely dense regions reaching  $\delta_{\text{QSO}} \sim 23$ , whereas Case B exhibits a comparatively moderate maximum of  $\delta_{\text{QSO}} \sim 10$ . This discrepancy suggests the possibility that sample selection effects may enhance the visibility of such extremely high density regions. These findings highlight the inadequacy of the Gaussian assumption in the extreme tail. In contrast, the AGND model provides an excellent fit across the full range of CIC counts. This result demonstrates that Gaussian fitting is inadequate for evaluating quasar overdensities in the high-density regime, whereas the AGND model offers a more accurate and physically motivated description of the underlying distribution. Because Y. Liang et al. (2025) evaluated the CH overdensity using a Gaussian fit, this comparison

is essential for reassessing the claimed statistical significance of the CH. This result also underpins our later conclusion (Section 4) that the CH is more probable within  $\Lambda$ CDM than implied by a Gaussian-based analysis. The best-fit parameters of the Gaussian model and the AGND model are given in Table 3.

### 3.6. NND analysis of quasars

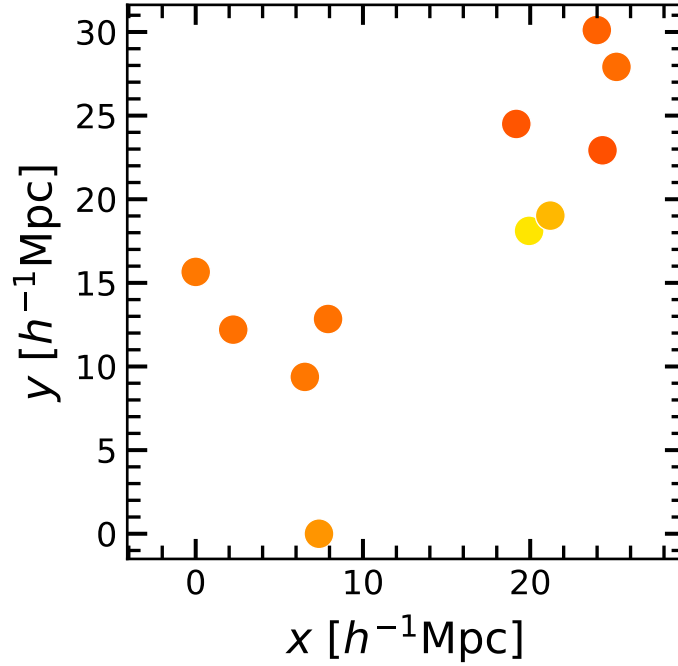
As a next step for quantifying quasar clustering, we employ the nearest-neighbor distribution (NND). The NND is defined as the probability distribution of the distance  $r$  from an object to its closest neighbor. It can be characterized by the cumulative distribution function (CDF),  $P_{\text{NN}}(< r)$ , which gives the probability that the nearest neighbor lies within distance  $r$ . The corresponding probability density function (PDF) is  $p_{\text{NN}}(r) = \frac{dP_{\text{NN}}(< r)}{dr}$ . An excess probability at small separations—i.e., a higher  $P_{\text{NN}}(< r)$  at small  $r$  relative to a random distribution—indicates a population that is more strongly clustered.

To quantify clustering in localized regions, we focus on the NND calculated for the most quasar-overdense cell identified by the CIC analysis for each Type I AGN sample realization. Figure 5 presents the projection maps of the quasar distributions. Panel (a) shows the distribution in the CH, while panels (b) and (c) display examples of a single Type I AGN sample realization for Case A and Case B, respectively. The NND was then calculated for the quasars within these extreme overdensities. However, a direct comparison of NNDs across samples and the observation (CH) is problematic because NND fundamentally depends on the number density of the target objects, which varies significantly across datasets.

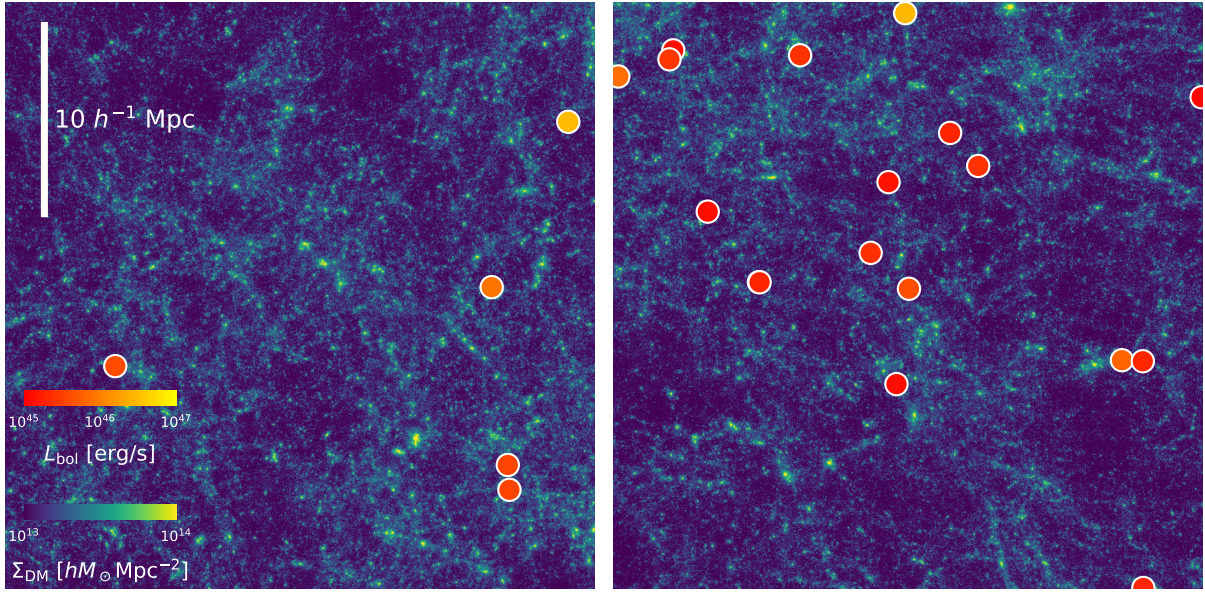
To overcome this limitation and enable a robust comparison, we model  $P_{\text{NN}}(< r)$  by incorporating a power-law two-point correlation function (TPCF;  $\xi(r)$ ), which describes the excess probability of finding a pair at a separation  $r$ . The probability of *NOT* finding a pair within a distance  $r$  denoted as  $P_{\text{NN}}(> r)$ , is related to the TPCF by the following expression (S. N. Chiu 2013):

$$P_{\text{NN}}(> r) = \exp\left(-\int_0^r 4\pi r'^2 \bar{n}(1 + \xi(r')) dr'\right), \quad (18)$$

where  $\bar{n}$  is the cosmic mean number density of objects. Consequently, the cumulative NND  $P_{\text{NN}}(< r)$  is given



(a) The Cosmic Himalayas



(b) Case A

(c) Case B

**Figure 5.** Projection maps of quasar distributions.

(a) The observed quasar distribution in the Cosmic Himalayas (CH) (Y. Liang et al. 2025), shown in the comoving frame where  $(x, y)$  represents the comoving coordinates relative to the fiducial point. This  $\sim (30 h^{-1} \text{Mpc})^3$  region contains 11 quasars. Points represent quasars, color-coded by their bolometric luminosity using the same normalization and color scale as shown in panels (b).

(b) An example of a candidate region for a CH analog in the Case A selection (containing 5 quasars). This distribution corresponds to the most overdense cell identified in a single random realization of the Type I AGN selection. Points represent quasars, color-coded by their bolometric luminosity calculated from Equation (8), and the background color shows the projected dark matter column density.

(c) An example of a CH analog in the Case B selection (containing 17 quasars), similarly extracted from a single realization of the Type I selection. The color coding and background are identical to those in panel (b).

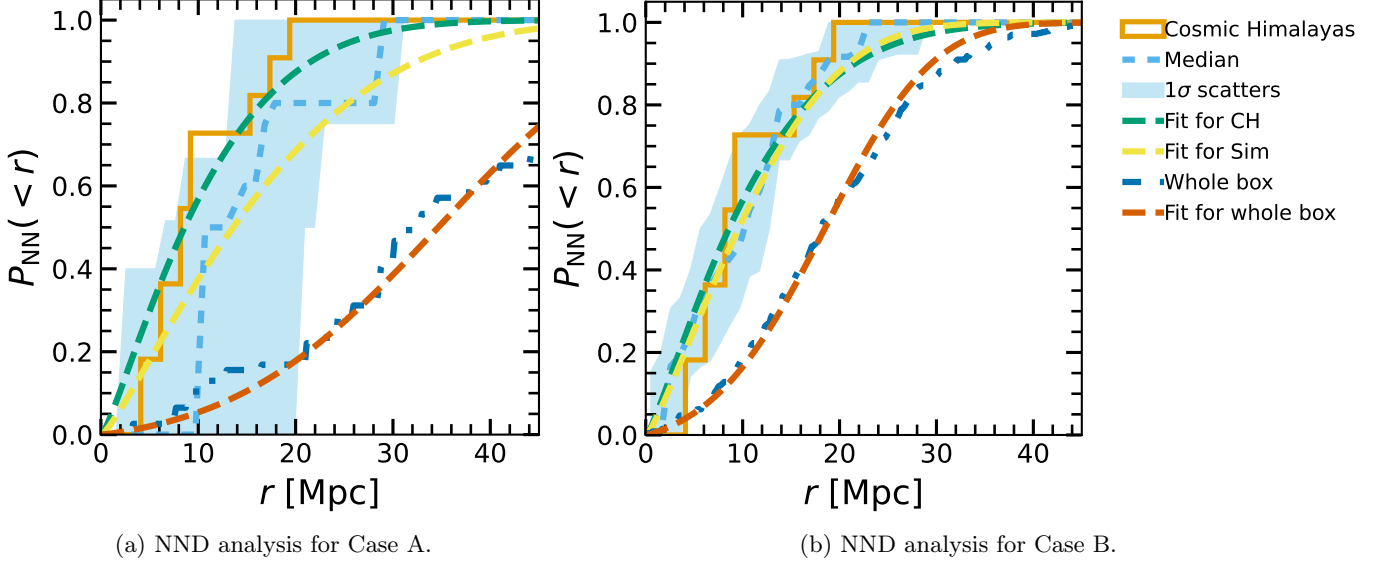


**Figure 6.** Nearest-neighbor distribution (NND) analysis results. The orange line shows the NND of quasars in the CH. The sky-blue line with shaded region represents the NND of the most overdense quasar regions, identified through CIC analysis in each Type-I AGN sample realization for each selection case (BF50NEL). Specifically, the associated shade indicates the  $1\sigma$  scatter obtained by the 100 jackknife trials (16th–84th percentile). The blue dotted line shows an example of the NND calculated for the entire  $200 h^{-1}$  Mpc simulation box in a trial. At first glance, the NND of the CH appears to show excellent agreement with Case B, whereas Case A shows a clear deviation. However, these apparent similarities and deviations stem primarily from differences in the mean quasar number density rather than intrinsic clustering signals. To address this, we quantify the intrinsic clustering strength (correlation length  $r_0$ ) by fitting the NND using the formulation derived in Equation (20). The green, yellow, and red dotted lines present the fitting results of the NND via single power-law model of the TPCF  $\xi(r) = (r/r_0)^{-\gamma}$ , with a fixed slope of  $\gamma = 1.8$ . Specifically, the green line corresponds to the fitting result for the CH, the yellow line for the most overdense regions in our simulation, and the red line for the NND of the whole simulation box. The correlation lengths by these fittings are summarized in Table 4.

**Table 4.** Correlation length estimated by the fitting of NND.

$r_0$ [ $h^{-1}$ Mpc]	CH	Case A	Case B
Extreme overdensities	29.4	30.9	13.7
whole box	–	8.36	4.97

by:

$$P_{\text{NN}}(< r) = 1 - P(> r) \quad (19)$$

$$= 1 - \exp\left(-\int_0^r 4\pi r'^2 \bar{n}(1 + \xi(r')) dr'\right). \quad (20)$$

Using this relation, we can isolate the clustering signature (encoded in  $\xi(r)$ ) from the number density effects.

To quantify the clustering strength using this formulation, we fit this analytical model to the observed  $P_{\text{NN}}(< r)$  from our simulations and the observation (CH), using a single power-law TPCF,  $\xi(r) = (r/r_0)^{-\gamma}$ , with the power-law index fixed to the standard value of  $\gamma = 1.8$ . This approach allows us to determine the correlation length  $r_0$ , which effectively quantifies the clustering strength independent of the sample density.

Figure 6 shows the NND analysis results for Case A and Case B. At first glance, the NND of the CH appears to show excellent agreement with Case B, whereas Case A shows a clear deviation. However, we must caution that a direct comparison of  $P_{\text{NN}}(< r)$  is misleading because the cosmic mean number density of quasars varies significantly between samples. To address this, we quantify the intrinsic clustering strength (correlation length  $r_0$ ) using the formulation derived in Equation (20).

Through this fitting procedure, we obtained the correlation lengths listed in Table 4. Notably, our analysis reveals that the apparent agreement between Case B and the CH is driven primarily by the higher number density in the Case B selection, rather than by intrinsic clustering properties. In contrast, when correcting for density effects, the correlation length derived for the Case A selection ( $r_0 \simeq 30 h^{-1}$  Mpc) is consistent with that of the CH. Regarding the similarities between the simulated cases, both Case A and Case B exhibit significant spatial variations in clustering strength; depending on the specific cell selection, the derived  $r_0$  can vary by a factor of  $\sim 3$  relative to the global trend. These findings support our CIC results, suggesting that the strong clustering signals similar to the CH naturally emerge from the combined effects of sample selection biases and cosmic variance.

#### 4. DISCUSSION

To clarify the origin of the extreme peak-height value ( $\nu = \delta/\sigma = 16.9$ ) argued for CH, we performed the

CIC analyses on our simulation samples. It is important to highlight the methodological differences between our analysis and that of Y. Liang et al. (2025). First, our simulation box has a size of  $L_{\text{box}} = 200 h^{-1}$  Mpc  $\simeq 295$  Mpc, whereas the SDSS observational fields span Gpc-scale volumes. Second, Y. Liang et al. (2025) divided the survey into a fixed grid, which risks splitting intrinsically dense regions across multiple cells and diluting the signal. By contrast, we considered both  $(L_{\text{box}}/L_{\text{cell}})^3 \approx (200/30)^3 \sim 3 \times 10^2$  independent non-overlapping cells and overlapping random placements to obtain a smoother estimate of the PDF shape. This approach is well-suited to constraining the functional form of the CIC distribution, though it cannot by itself capture the survey-wide tail statistics expected in Gpc-scale fields.

The fundamental mode of the box is  $k_f = 2\pi/L_{\text{box}} \approx 0.031 h \text{ Mpc}^{-1}$ , comparable to  $1/L_{\text{cell}}$ . Thus, the modes that dominate fluctuations within a  $30 h^{-1}$  Mpc cell—which set the skewness and tail of the one-point distribution—are well sampled by many higher- $k$  modes inside the box. In other words, the  $200 h^{-1}$  Mpc volume is sufficient to determine the *shape* of  $P_{\text{CIC}}(N_{\text{QSO}}; L_{\text{cell}})$ , even if it cannot measure the absolute rarity of the most extreme cells across a Gpc-scale survey.

On Gpc-scale volumes, even mild non-Gaussianity in the true CIC probability distribution function can make a “ $\sigma$ -language” summary a misleading exaggeration of the PDF tail. Our simulation shows that the quasar CIC is distinctly non-Gaussian; a Gaussian with a fixed mean fails to reproduce the high- $N_{\text{QSO}}$  tail, whereas the AGND model provides an excellent fit, consistent with the results for dark matter haloes reported by J. Shin et al. (2017). Thus, the reported “ $16.9\sigma$ ” significance corresponds to an incorrect likelihood model, and  $\sigma$ -equivalents lose their interpretive meaning when the assumed likelihood is wrong. We explicitly demonstrated this Gaussian mis-fit and the successful AGND fit in Figure 4.

A more appropriate metric is the exceedance probability under the fitted non-Gaussian PDF:

$$p_{\geq N_*} = \sum_{N=N_*}^{\infty} P_{\mathcal{N}_{\nu,2}}(N; L_{\text{cell}}), \quad (21)$$

where  $N_*$  serves as a threshold count. This metric  $p_{\geq N_*}$  represents the probability of finding  $N_{\text{QSO}} \geq N_*$  quasars within a single cell. This probability can then be converted into a survey-level probability using the effective number of independent cells,  $\zeta$ :

$$P_{\text{exist}}(N_{\text{QSO}} \geq N_*, V_{\text{survey}}) = 1 - (1 - p_{\geq N_*})^{\zeta}, \quad (22)$$

where  $\zeta \approx (V_{\text{survey}}/L_{\text{cell}}^3)$ .

In other words,  $p_{\geq N_*}$  given in Equation (21), is the cell-level exceedance probability that one random cell of size  $L_{\text{cell}}$  has at least  $N_*$  quasars; i.e., it tells us how rare such a cell is locally. The latter term in Equation (22),  $(1-p_{\geq N_*})^\zeta$ , represents the probability that none of the  $\zeta$  cells exceeds the threshold. Then, Equation (22) represents the complement, i.e., the probability that at least one cell in the survey exceeds the threshold  $N_*$ . This indicates the likelihood that the survey will contain at least one such cell, given its vast volume.

We first applied this formulation to the Case A samples, which exhibit a mean quasar number density similar to the SDSS survey (Y. Liang et al. 2025). We set the threshold to  $N_* = 8$ , which corresponds to the highly overdense regime of  $\delta_{\text{QSO}} \gtrsim 17\sigma_{\text{Gauss}}$ . With the parameters set as  $L_{\text{cell}} = 30 h^{-1}\text{Mpc}$ , and a survey volume of  $V_{\text{survey}} = 1 h^{-3}\text{Gpc}^3$ , the probability of finding at least one such cell is  $P_{\text{exist}} = 0.71$ , computed using the fitted AGND parameters in Table 3, with  $p_{\geq N_*} \approx 3.306 \times 10^{-5}$  and  $\zeta = 37,037$ . When the survey volume is increased to  $V_{\text{survey}} = (2 h^{-1}\text{Gpc})^3$ , it rises to  $P_{\text{exist}} \approx 1$ , with  $\zeta = 296,296$  and the same value of  $p_{\geq N_*}$ .

Next, we examined the Case B samples. We set the threshold to  $N_* = 25$ , which again corresponds to the extreme overdensity level of  $\delta \gtrsim 17\sigma_{\text{Gauss}}$ . With the same cell size ( $L_{\text{cell}} = 30 h^{-1}\text{Mpc}$ ) and a survey volume of  $V_{\text{survey}} = 1 h^{-3}\text{Gpc}^3$ , it yields a probability of  $P_{\text{exist}} = 0.024$  with  $p_{\geq N_*} \approx 6.5316 \times 10^{-6}$ . Increasing the survey volume to  $V_{\text{survey}} = (2 h^{-1}\text{Gpc})^3$  increases this probability to  $P_{\text{exist}} = 0.18$ .

While a more detailed treatment of the quasar selection function is beyond the scope of this paper, these results strongly support the notion that the emergence of extreme overdense regions, such as the CH, is a natural consequence in a Gpc-scale survey like SDSS. Crucially, the clear difference in the realization probability between Case A and Case B demonstrates that the selection criteria significantly influence the observed emergence of these high-density regions.

Finally, we acknowledge that this study has focused primarily on the statistical properties of quasar distributions. We have not explicitly investigated the underlying dark matter environments of the identified CH analogs to determine whether they physically reside within genuine protoclusters. Consequently, while we confirm that the extreme quasar overdensity is statistically consistent with  $\Lambda\text{CDM}$ , it remains an open question whether the CH explicitly traces the most massive dark matter structures at this redshift. A detailed examination of the halo environments hosting these CH analogs is reserved for future work.

In summary, this study provides a crucial revision to the conventional assessment of extreme overdensities. We have demonstrated that the Gaussian model is fundamentally inadequate for quantifying quasar overdensities in the high-density regime because it fails to capture the significant skewness and heavy-tailed nature of the underlying CIC distribution. To resolve this, we employed a novel framework based on the AGND model. This framework is robust because it (i) respects the correct heavy-tailed form measured directly in our simulations, and (ii) scales naturally to the Gpc-scale volume of the SDSS survey. Crucially, our NND analysis further supports this conclusion by revealing that regions exhibiting two-point clustering properties highly analogous to the CH (termed CH analogs) naturally emerge within our simulation volume. This finding suggests that the observed strong clustering signal is not an anomalous effect but rather a plausible consequence of the combined effects of sample selection biases (as modeled by our Case A and Case B criteria) and the inherent cosmic variance. Applying this robust method reveals that the rarity of the observed extreme structure, such as the CH, is substantially lower than the often-cited Gaussian-based ‘ $\sim 17\sigma$ ’ claim. By accurately modeling the underlying distribution, our results successfully reconcile the existence of the CH with expectations from the standard  $\Lambda\text{CDM}$  paradigm.

## 5. SUMMARY

In this paper, we investigated the emergence and properties of extreme quasar overdensities using the *CROCODILE* cosmological hydrodynamic simulations, examining them from both large-scale (CIC) and small-scale (NND) perspectives. Our simulation provides BH masses and accretion rates, from which we estimated quasar luminosities. The resulting BH population is consistent with those of other simulations and observations of Eddington ratios, X-ray luminosity, and BH mass function (Figures 1–3). Based on these samples, we selected quasars according to mass- and luminosity-based criteria (Cases A and B) and analysed their clustering properties.

From our CIC analysis, we find that the observed distribution of quasar counts deviates strongly from the Gaussian assumption, particularly in the high-density tail. As a consequence, conventional Gaussian fits systematically overestimate the rarity of extreme overdensities (e.g., inferring  $\delta \sim 12\sigma_{\text{Gauss}}$  for simulated overdense cells that are actually more common), whereas a non-Gaussian functional form, such as the AGND model, provides a significantly more accurate description across the full range of counts. Both Case A and B high-

light this effect, with the more biased selection (Case A) exhibiting the largest discrepancy. We reinforced this finding by calculating the exceedance probability using the AGND model in both the *CROCODILE* simulation (Sec 4) and the *Uchuu* simulation (appendix A which has a much larger boxsize of  $2h^{-1}$  Gpc. Our CIC results therefore imply that the CH overdensity has been substantially overstated.

For further investigation into the physical origin of the strong clustering, we perform the NND analysis, which allows us to quantify the two-point statistics highly localized, small regions. By connecting the NND with TPCF, we find that the strong clustering signature observed in the CH ( $r_0 \sim 30h^{-1}$  Mpc) naturally arises in samples from Case A, which represents a more biased sample selection. This result strongly supports the statement that the extreme clustered regions of quasars emerge from the compound effect of sample selection biases and the spatial dependence of the observed field, thus implicating sample selections and cosmic variance as the primary drivers.

In summary, the apparent tension between the existence of extreme structures (like CH analogs) in  $\Lambda$ CDM simulations and the extreme overdensity reported by Y.

Liang et al. (2025) stems from the inappropriate use of a Gaussian assumption for the CIC distribution. Once the correct non-Gaussian functional form is adopted, the inferred rarity of the Cosmic Himalayas is substantially reduced, allowing the simulation adopting the standard universe model to successfully observe these extreme overdensities. Complementing this, our NND analysis confirms that strong clustering signals can be observed due to the compound effect of sample selection biases (as modeled by Case A and Case B) and cosmic variance. These findings conclusively support our conclusion that the extreme overdensity and clustering of quasars can be naturally produced within the  $\Lambda$ CDM framework.

#### ACKNOWLEDGMENTS

This work used computational resources of the SQUID provided by the D3 Center of the University of Osaka, through the HPCI System Research Project (Project IDs: hp240141, hp250119). This work is partially supported by the MEXT/JSPS KAKENHI Grant Numbers 22K21349, 24H00002, 24H00241, 25K01032 (K.N.) and 21H04489 (H.Y.) and JST FOREST Program Grant Number JP-MJFR202Z (H.Y.).

## APPENDIX

### A. COUNT-IN-CELLS (CIC) ANALYSIS IN THE *UCHUU* SIMULATION

To validate the robustness of our findings based on the *CROCODILE* simulation box, we carried out a complementary CIC analysis using the cosmological  $N$ -body simulation *Uchuu* (T. Ishiyama et al. 2021), which spans a comoving volume of  $L_{\text{box}} = 2h^{-1}$  cGpc. The *Uchuu* simulation provides an ideal large-volume counterpart for testing whether the functional form and tail behavior of the CIC distribution inferred from the *CROCODILE* box remain valid at Gpc scales, although we need a model to assign quasars to dark matter haloes as we describe below.

In Case C, we select halos with  $\log_{10}(M_{200c}/M_{\odot}) > 11.5$ , corresponding to typical hosts of black holes in the range  $7.1 < \log_{10}(M_{\text{BH}}/M_{\odot}) < 9.9$ , consistent with our Case B selection. The mapping between halo mass and BH mass was derived from the  $M_{\text{BH}} - M_*$  relation of Y. Zhang et al. (2023) combined with the  $M_{\text{h}} - M_*$  relation at  $z = 2.0$  from P. S. Behroozi et al. (2013), as illustrated in Figure 7. For this halo sample, we incorporate the observed dependence of AGN host occurrence on halo mass (S. B. Rembold et al. 2023), as shown in Figure 8. The AGN fraction is modeled as a function of halo mass using an AGND model, whose amplitude was scaled such that the resulting sample yields a mean halo count per cell of  $\bar{N}_{\text{halo}} \simeq 0.36$ . This fitting function is applied as a probability weight to downsample the halo catalog, ensuring that the resulting halo population reproduces the observed AGN occupation fraction. The best-fit AGND parameters of the observed AGN occupation fraction are  $\alpha = 2.2467$ ,  $\kappa = -0.1999$ , and  $\xi = 12.8270$ , shown as the green long-dashed line in Figure 8. The subsequent CIC analysis is performed on this downsampled halo sample, employing the randomly selected cell placement scheme ( $N_{\text{cell}} = 10^9$ ) described in Sec. 3.5.

Figure 9 presents the resulting CIC distributions for reduced haloes in the *Uchuu* simulation. As in our *CROCODILE* analysis, the Gaussian fit fails to reproduce the asymmetric and heavy-tailed shapes of the simulated distributions, whereas the AGND fit provides an excellent description across the full range of counts. This effect reproduces the unrealistically high- $N$  regime ( $\delta_{\text{halo}}^{\text{max}} \sim 24 \sim 16.6\sigma_{\text{Gauss}}$ ) under the Gaussian assumption. The corresponding best-fit parameters are listed in Table 5.

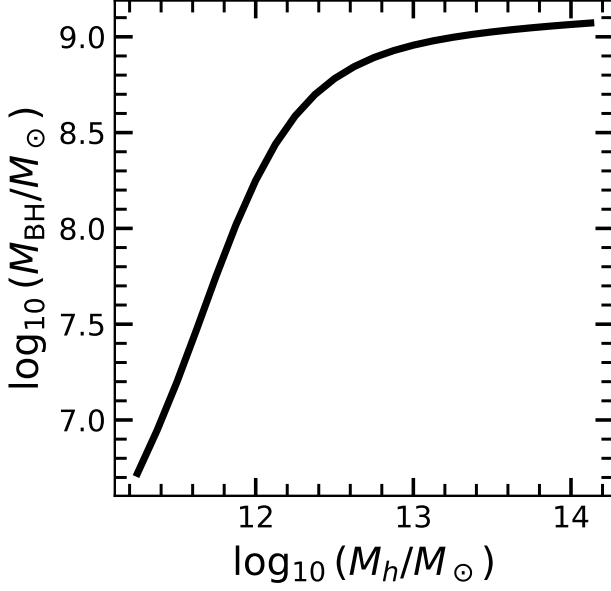


**Figure 7.** BH mass–halo mass relation at  $z \sim 2$ . The relation is derived by combining the  $M_*$ – $M_h$  relation from P. S. Behroozi et al. (2013) at  $z \sim 2$  with the  $M_*$ – $M_{\text{BH}}$  relation from Y. Zhang et al. (2023).

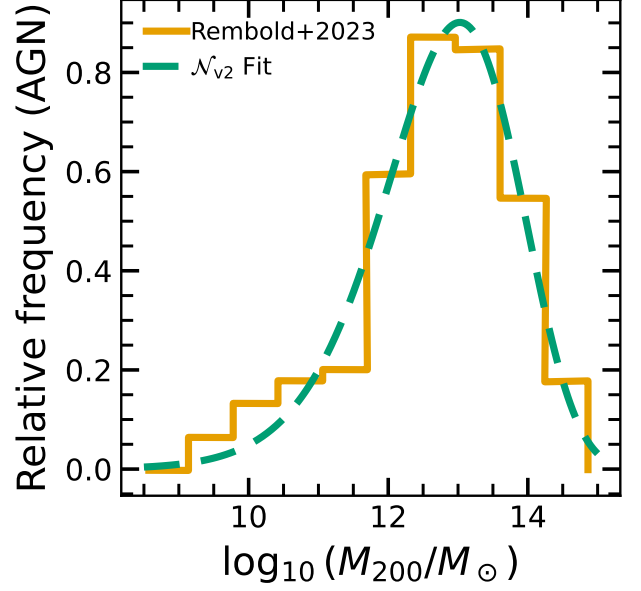


**Figure 8.** Relative AGN frequency as a function of halo mass. The orange histogram shows the observational results from S. B. Rembold et al. (2023), while the green dashed line represents the AGND fit to this relation. This empirical relation was used to downsample the halo population in Case C to match the observed AGN occupation fraction.

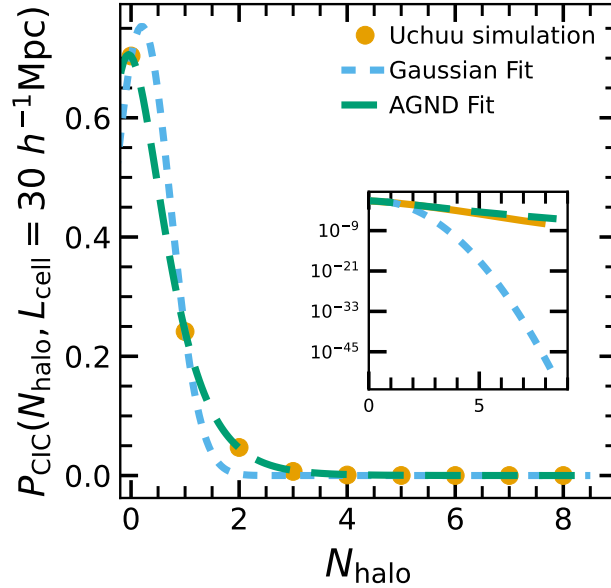


**Figure 9.** CIC probability distribution of quasar-host haloes for  $L_{\text{cell}} = 30 h^{-1} \text{Mpc}$ . The orange points show the CIC measured from the *Uchuu* simulation (T. Ishiyama et al. 2021). The blue dashed curve corresponds to a Gaussian fit, while the green long-dashed curve shows the AGND fit. The inset panel presents the same distributions on a semi-log scale, highlighting the deviations between the Gaussian model and the simulation results in the high- $\delta$  regime.

The result from this Gpc-scale analysis demonstrates that the non-Gaussian form of the CIC distribution persists in much larger volumes, confirming the robust existence of extreme quasar overdensities.

**Table 5.** Best-fit parameters of the Gaussian and AGND model describing the halo CIC probability distributions in the *Uchuu* simulation.

Gaussian	$\mu$	$\sigma$	AGND	$\alpha$	$\kappa$	$\xi$
Case C	0.2005	0.5294	Case C	0.6161	0.4162	0.1902

## B. THE CIC RESULTS FROM DIFFERENT SIMULATIONS

To clarify the dependence of results on simulations, we applied the CIC analysis to the samples with wider mass ranges. For BF50NEL and *Uchuu*, we selected haloes satisfying  $\log_{10}(M_h/M_\odot) > 11.5$  and utilized the data at  $z = 2.2$ , consistent with the redshift of our main analysis. Regarding Shin+2017, we utilized the data from J. Shin et al. (2017) at  $z = 0$  as a substitute, since the CIC distribution at  $z \sim 2$  was not reported in their study.

Figure 10 shows the difference in the CIC for different simulations. The simulation of J. Shin et al. (2017) has a narrower distribution due to a higher resolution than ours and can model lower mass haloes. The CIC analysis of *Uchuu* is based on the grid-based method, whereas random sampling ( $N_{\text{cell}} = 10^6$ ) was used for BF50NEL. The comparison demonstrates rough consistency in the derived quasar population in all simulations.

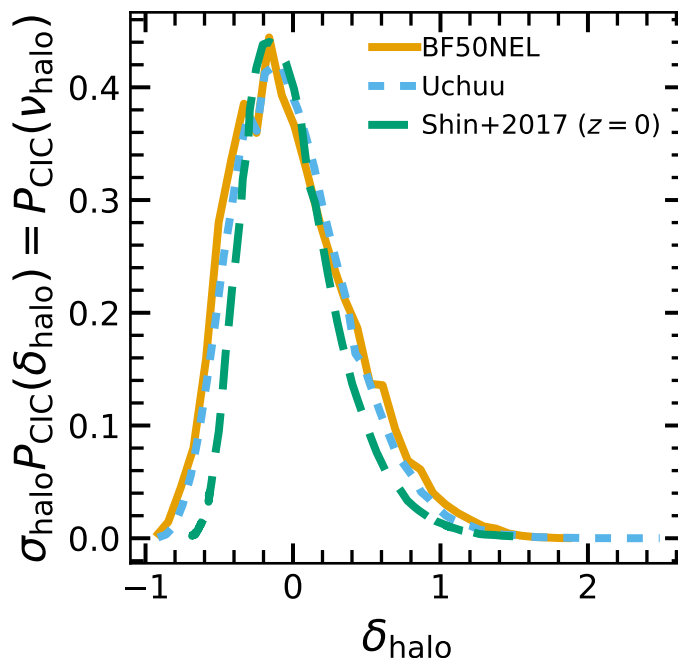


**Figure 10.** The CIC probability distribution for halos in three different simulations: BF50NEL with  $\log_{10} M_h/M_\odot > 11.5$  (orange line), the *Uchuu* simulation with  $\log_{10} M_h/M_\odot > 11.5$  (skyblue dashed line), and  $z = 0$  data from J. Shin et al. (2017) (green long-dashed). For BF50NEL and the *Uchuu*, we took cubic cells with  $L_{\text{cell}} = 30 h^{-1}\text{Mpc}$ , while spheres with a radius  $R_{\text{th}} = 25 h^{-1}\text{Mpc}$  were used for J. Shin et al. (2017).

## REFERENCES

- Aird, J., Coil, A. L., & Georgakakis, A. 2018, Monthly Notices of the Royal Astronomical Society, 474, 1225, doi: [10.1093/mnras/stx2700](https://doi.org/10.1093/mnras/stx2700)
- Aird, J., Coil, A. L., Georgakakis, A., et al. 2015, Monthly Notices of the Royal Astronomical Society, 451, 1892, doi: [10.1093/mnras/stv1062](https://doi.org/10.1093/mnras/stv1062)
- Andrews, M., Artale, M. C., Kumar, A., et al. 2025, A&A, 698, A280, doi: [10.1051/0004-6361/202452628](https://doi.org/10.1051/0004-6361/202452628)
- Angulo, R. E., & Pontzen, A. 2016, Monthly Notices of the Royal Astronomical Society: Letters, 462, L1, doi: [10.1093/mnrasl/slw098](https://doi.org/10.1093/mnrasl/slw098)
- Banerjee, A., & Abel, T. 2021, MNRAS, 500, 5479, doi: [10.1093/mnras/staa3604](https://doi.org/10.1093/mnras/staa3604)
- Behroozi, P. S., Wechsler, R. H., & Conroy, C. 2013, The Astrophysical Journal, 770, 57, doi: [10.1088/0004-637X/770/1/57](https://doi.org/10.1088/0004-637X/770/1/57)

- Blas, D., Lesgourgues, J., & Tram, T. 2011, *Journal of Cosmology and Astroparticle Physics*, 2011, 034, doi: [10.1088/1475-7516/2011/07/034](https://doi.org/10.1088/1475-7516/2011/07/034)
- Buchner, J., Georgakakis, A., Nandra, K., et al. 2015, *The Astrophysical Journal*, 802, 89, doi: [10.1088/0004-637X/802/2/89](https://doi.org/10.1088/0004-637X/802/2/89)
- Chiang, Y.-K., Overzier, R., & Gebhardt, K. 2013, *The Astrophysical Journal*, 779, 127, doi: [10.1088/0004-637X/779/2/127](https://doi.org/10.1088/0004-637X/779/2/127)
- Chiu, S. N. 2013, *Stochastic geometry and its applications*, 3rd edn., Wiley series in probability and mathematical statistics
- Crain, R. A., Schaye, J., Bower, R. G., et al. 2015, *Monthly Notices of the Royal Astronomical Society*, 450, 1937, doi: [10.1093/mnras/stv725](https://doi.org/10.1093/mnras/stv725)
- Croft, R., Shaw, P., Alexis, A.-M., et al. 2025, *The Open Journal of Astrophysics*, 8, 124, doi: [10.33232/001c.143599](https://doi.org/10.33232/001c.143599)
- Davé, R., Anglés-Alcázar, D., Narayanan, D., et al. 2019, *Monthly Notices of the Royal Astronomical Society*, 486, 2827, doi: [10.1093/mnras/stz937](https://doi.org/10.1093/mnras/stz937)
- Dubois, Y., Pichon, C., Welker, C., et al. 2014, *Monthly Notices of the Royal Astronomical Society*, 444, 1453, doi: [10.1093/mnras/stu1227](https://doi.org/10.1093/mnras/stu1227)
- Ferland, G. J., Porter, R. L., van Hoof, P. a. M., et al. 2013, *Revista Mexicana de Astronomia y Astrofisica*, 49, 137, doi: [10.48550/arXiv.1302.4485](https://doi.org/10.48550/arXiv.1302.4485)
- García-Vergara, C., Hennawi, J. F., Barrientos, L. F., & Rix, H.-W. 2017, *The Astrophysical Journal*, 848, 7, doi: [10.3847/1538-4357/aa8b69](https://doi.org/10.3847/1538-4357/aa8b69)
- García-Vergara, C., Rybak, M., Hodge, J., et al. 2022, *The Astrophysical Journal*, 927, 65, doi: [10.3847/1538-4357/ac469d](https://doi.org/10.3847/1538-4357/ac469d)
- Gaspari, M., Ruszkowski, M., & Oh, S. P. 2013, *Monthly Notices of the Royal Astronomical Society*, 432, 3401, doi: [10.1093/mnras/stt692](https://doi.org/10.1093/mnras/stt692)
- Georgakakis, A., Aird, J., Schulze, A., et al. 2017, *Monthly Notices of the Royal Astronomical Society*, 471, 1976, doi: [10.1093/mnras/stx1602](https://doi.org/10.1093/mnras/stx1602)
- Haardt, F., & Madau, P. 2012, *The Astrophysical Journal*, 746, 125, doi: [10.1088/0004-637X/746/2/125](https://doi.org/10.1088/0004-637X/746/2/125)
- Habouzit, M., Li, Y., Somerville, R. S., et al. 2021, *Monthly Notices of the Royal Astronomical Society*, 503, 1940, doi: [10.1093/mnras/stab496](https://doi.org/10.1093/mnras/stab496)
- Habouzit, M., Somerville, R. S., Li, Y., et al. 2022, *Monthly Notices of the Royal Astronomical Society*, 509, 3015, doi: [10.1093/mnras/stab3147](https://doi.org/10.1093/mnras/stab3147)
- Hahn, O., Rampf, C., & Uhlemann, C. 2021, *Monthly Notices of the Royal Astronomical Society*, 503, 426, doi: [10.1093/mnras/staa3773](https://doi.org/10.1093/mnras/staa3773)
- Hatch, N. A., Wylezalek, D., Kurk, J. D., et al. 2014, *Monthly Notices of the Royal Astronomical Society*, 445, 280, doi: [10.1093/mnras/stu1725](https://doi.org/10.1093/mnras/stu1725)
- Hopkins, P. F., Richards, G. T., & Hernquist, L. 2007, *The Astrophysical Journal*, 654, 731, doi: [10.1086/509629](https://doi.org/10.1086/509629)
- Ishiyama, T., Prada, F., Klypin, A. A., et al. 2021, *Monthly Notices of the Royal Astronomical Society*, 506, 4210, doi: [10.1093/mnras/stab1755](https://doi.org/10.1093/mnras/stab1755)
- Laloux, B., Georgakakis, A., Alexander, D. M., et al. 2024, *Monthly Notices of the Royal Astronomical Society*, 532, 3459, doi: [10.1093/mnras/stae1649](https://doi.org/10.1093/mnras/stae1649)
- Liang, Y., Ouchi, M., Sun, D., et al. 2025, *The Astrophysical Journal*, Volume 986, Issue 1, id.60, 16 pp., 986, 60, doi: [10.3847/1538-4357/adc1bb](https://doi.org/10.3847/1538-4357/adc1bb)
- Lim, S., Scott, D., Babul, A., et al. 2021, *MNRAS*, 501, 1803, doi: [10.1093/mnras/staa3693](https://doi.org/10.1093/mnras/staa3693)
- Merloni, A., Bongiorno, A., Brusa, M., et al. 2014, *Monthly Notices of the Royal Astronomical Society*, 437, 3550, doi: [10.1093/mnras/stt2149](https://doi.org/10.1093/mnras/stt2149)
- Michaux, M., Hahn, O., Rampf, C., & Angulo, R. E. 2021, *Monthly Notices of the Royal Astronomical Society*, 500, 663, doi: [10.1093/mnras/staa3149](https://doi.org/10.1093/mnras/staa3149)
- Mignoli, M., Gilli, R., Decarli, R., et al. 2020, *Astronomy and Astrophysics*, 642, L1, doi: [10.1051/0004-6361/202039045](https://doi.org/10.1051/0004-6361/202039045)
- Nelson, D., Pillepich, A., Springel, V., et al. 2018, *Monthly Notices of the Royal Astronomical Society*, 475, 624, doi: [10.1093/mnras/stx3040](https://doi.org/10.1093/mnras/stx3040)
- Oku, Y., & Nagamine, K. 2024, *The Astrophysical Journal*, 975, 183, doi: [10.3847/1538-4357/ad77d3](https://doi.org/10.3847/1538-4357/ad77d3)
- Oku, Y., Tomida, K., Nagamine, K., Shimizu, I., & Cen, R. 2022, *The Astrophysical Journal Supplement Series*, 262, 9, doi: [10.3847/1538-4365/ac77ff](https://doi.org/10.3847/1538-4365/ac77ff)
- Ouellette, A., & Holder, G. 2025, *arXiv e-prints*, arXiv:2502.09709, doi: [10.48550/arXiv.2502.09709](https://doi.org/10.48550/arXiv.2502.09709)
- Overzier, R. A. 2016, *Astronomy and Astrophysics Review*, 24, 14, doi: [10.1007/s00159-016-0100-3](https://doi.org/10.1007/s00159-016-0100-3)
- Planck Collaboration, Aghanim, N., Akrami, Y., et al. 2020, *Astronomy & Astrophysics*, 641, A6, doi: [10.1051/0004-6361/201833910](https://doi.org/10.1051/0004-6361/201833910)
- Rakshit, S., Stalin, C. S., & Kotilainen, J. 2020, *The Astrophysical Journal Supplement Series*, 249, 17, doi: [10.3847/1538-4365/ab99c5](https://doi.org/10.3847/1538-4365/ab99c5)
- Rembold, S. B., Riffel, R., Riffel, R. A., et al. 2023, *Monthly Notices of the Royal Astronomical Society*, 527, 6722, doi: [10.1093/mnras/stad3584](https://doi.org/10.1093/mnras/stad3584)
- Remus, R.-S., Dolag, K., & Dannerbauer, H. 2023, *ApJ*, 950, 191, doi: [10.3847/1538-4357/acbb91](https://doi.org/10.3847/1538-4357/acbb91)

- Richarte, M. G., Toscano, F., Garcia Lambas, D., et al. 2025, *Astronomy and Astrophysics*, 700, A269, doi: [10.1051/0004-6361/202554998](https://doi.org/10.1051/0004-6361/202554998)
- Romano, L. E. C., Nagamine, K., & Hirashita, H. 2022a, *Monthly Notices of the Royal Astronomical Society*, 514, 1441, doi: [10.1093/mnras/stac1385](https://doi.org/10.1093/mnras/stac1385)
- Romano, L. E. C., Nagamine, K., & Hirashita, H. 2022b, *Monthly Notices of the Royal Astronomical Society*, 514, 1461, doi: [10.1093/mnras/stac1386](https://doi.org/10.1093/mnras/stac1386)
- Rosas-Guevara, Y. M., Bower, R. G., Schaye, J., et al. 2015, *Monthly Notices of the Royal Astronomical Society*, 454, 1038, doi: [10.1093/mnras/stv2056](https://doi.org/10.1093/mnras/stv2056)
- Ryden, B. S., & Turner, E. L. 1984, *The Astrophysical Journal*, 287, L59, doi: [10.1086/184398](https://doi.org/10.1086/184398)
- Saitoh, T. R. 2017, *The Astronomical Journal*, 153, 85, doi: [10.3847/1538-3881/153/2/85](https://doi.org/10.3847/1538-3881/153/2/85)
- Schaye, J., Crain, R. A., Bower, R. G., et al. 2015, *Monthly Notices of the Royal Astronomical Society*, 446, 521, doi: [10.1093/mnras/stu2058](https://doi.org/10.1093/mnras/stu2058)
- Scoville, N., Aussel, H., Brusa, M., et al. 2007, *The Astrophysical Journal Supplement Series*, 172, 1, doi: [10.1086/516585](https://doi.org/10.1086/516585)
- Shin, J., Kim, J., Pichon, C., Jeong, D., & Park, C. 2017, *The Astrophysical Journal*, 843, 73, doi: [10.3847/1538-4357/aa74b9](https://doi.org/10.3847/1538-4357/aa74b9)
- Smith, B. D., Bryan, G. L., Glover, S. C. O., et al. 2017, *Monthly Notices of the Royal Astronomical Society*, 466, 2217, doi: [10.1093/mnras/stw3291](https://doi.org/10.1093/mnras/stw3291)
- Springel, V., Pakmor, R., Zier, O., & Reinecke, M. 2021, *Monthly Notices of the Royal Astronomical Society*, 506, 2871, doi: [10.1093/mnras/stab1855](https://doi.org/10.1093/mnras/stab1855)
- Suh, H., Scharwächter, J., Farina, E. P., et al. 2025, *Nature Astronomy*, 9, 271, doi: [10.1038/s41550-024-02402-9](https://doi.org/10.1038/s41550-024-02402-9)
- Toni, G., Gozaliasl, G., Maturi, M., et al. 2025, *Astronomy and Astrophysics*, 697, A197, doi: [10.1051/0004-6361/202553759](https://doi.org/10.1051/0004-6361/202553759)
- Trebitsch, M., Dubois, Y., Volonteri, M., et al. 2021, *A&A*, 653, A154, doi: [10.1051/0004-6361/202037698](https://doi.org/10.1051/0004-6361/202037698)
- Ueda, H., & Yokoyama, J. 1996, *Monthly Notices of the Royal Astronomical Society*, 280, 754, doi: [10.1093/mnras/280.3.754](https://doi.org/10.1093/mnras/280.3.754)
- Vogelsberger, M., Genel, S., Springel, V., et al. 2014, *Nature*, 509, 177, doi: [10.1038/nature13316](https://doi.org/10.1038/nature13316)
- Wylezalek, D., Vayner, A., Rupke, D. S. N., et al. 2022, *The Astrophysical Journal Letters*, 940, L7, doi: [10.3847/2041-8213/ac98c3](https://doi.org/10.3847/2041-8213/ac98c3)
- Yajima, H., Abe, M., Khochfar, S., et al. 2022, *Monthly Notices of the Royal Astronomical Society*, 509, 4037, doi: [10.1093/mnras/stab3092](https://doi.org/10.1093/mnras/stab3092)
- Yang, A., & Saslaw, W. C. 2011, *The Astrophysical Journal*, 729, 123, doi: [10.1088/0004-637X/729/2/123](https://doi.org/10.1088/0004-637X/729/2/123)
- Zhang, Y., Ouchi, M., Gebhardt, K., et al. 2023, *The Astrophysical Journal*, 948, 103, doi: [10.3847/1538-4357/acc2c2](https://doi.org/10.3847/1538-4357/acc2c2)
- Zhou, Z., Cisewski-Kehe, J., Fang, K., & Banerjee, A. 2025, *The Astrophysical Journal*, 979, 194, doi: [10.3847/1538-4357/ad924c](https://doi.org/10.3847/1538-4357/ad924c)